Supplementary Material

Modeling the evaporation of sessile multi-component droplets

C. Diddens[a], J.G.M. Kuerten[a,b], C.W.M. van der Geld[c], H.M.A. Wijshoff[a,d]

[a]Department of Mechanical Engineering, Eindhoven University of Technology, P.O. Box 513, 5600 MB Eindhoven, The Netherlands
[b]Faculty EEMCS, University of Twente, P.O. Box 217, 7500 AE Enschede, The Netherlands
[c]Department of Chemical Engineering and Chemistry, Eindhoven University of Technology, P.O. Box 513, 5600 MB Eindhoven, The Netherlands
[d]Océ-Technologies B.V., P.O. Box 101, 5900 MA Venlo, The Netherlands

Abstract

The supplementary information comprises an outline of the numerical algorithm, details of the finite element method, fits of experimental data to model the composition-dependence of the mixture properties, a discussion of drying mixture droplets with an unpinned contact line and details on the evaporation rate of mixture droplets.

S.1. Numerical implementation

The numerical implementation comprises the evaluation of the evaporation rates (12), the treatment of the height evolution (9), the determination of the velocities (u, w), the convection and diffusion of the mixture according to (2) and the corresponding change of the fields for the physical properties ρ, μ, σ and D_{AB}.

To solve the evaporation rate, there are three options: A direct calculation of $\dot{m}_\nu$ according to the analytical solution given in the supplementary material can be done, where the conical functions can be evaluated with the routines of Gil et al. [1]. Alternatively, the Laplace equation $\nabla^2 \hat{p} = 0$ with the corresponding boundary conditions can by solved directly (see Figure S.5) with a generalized version of the *AutoMUG* method described by

Shapira [2]. This is in particular useful if the vapor distribution in the air is of interest. Finally, the most stable and fastest method to obtain $\dot{m}_\nu$ is a boundary integral method that is outlined in the supplemenatry material. All three methods were used to validate each other (cf. section S.5.1).

The fluid composition y_ν and the physical properties are kept in a cell-centered volume-of-fluid grid, where the former are subject to (2) based on an explicit Euler integration with an (upwind) finite differences scheme. Since the height evolution (9) is a stiff integro-PDE, it is solved by a diagonally implicit Runge-Kutta method [3, 4]. The integrals in (9) and in the corresponding velocities are evaluated to the order of a linear interpolation between the grid points of ρ and μ. In order to solve (9) implicitly, a Newton scheme is used where the corresponding Jacobian with respect to h is evaluated numerically.

The interface delta function δ_Γ in the sink term of Eq. (2) is spread over the height of a single volume-of-fluid cell just below the interface. Since the top-most cells are generally not entirely filled with liquid, the mass fractions in the cells below are also partially affected.

The simulations in sections 3 and 4 were carried out on an anisotropic grid, where the distance to the initial contact line r_c and to the initial apex height $h(0,0)$ was discretized by 200×110 cells. We used a dynamically adjusted time step that ensures that the CFL number does not exceed 0.025.

S.2. Finite element method

For the FEM implementation in section 5, the Stokes flow (24) has to be converted to its axisymmetric weak form. Following the notation of the dimension reduction of Belhachmi et al. [5], we introduce

$$\nabla_\mathrm{a} \cdot \boldsymbol{v} = \partial_r u + \partial_z w \tag{S.1}$$

$$\mathbf{D_a}(\boldsymbol{v}) = \frac{1}{2} \begin{pmatrix} 2\partial_r u & \partial_r w + \partial_z u \\ \partial_r w + \partial_z u & 2\partial_z w \end{pmatrix} . \tag{S.2}$$

Multiplying (24) and (25) with test functions $\tilde{\boldsymbol{v}} = (\tilde{u}, \tilde{w})$ and $\tilde{p}$, respectively, and integrating by parts over the cross section of the droplet results in the following weak formulation:

$$a(\boldsymbol{v}, \tilde{\boldsymbol{v}}) - b(\tilde{\boldsymbol{v}}, p) = L(\tilde{\boldsymbol{v}}) \qquad \text{and} \qquad b(\boldsymbol{v}, \tilde{p}) = 0 \tag{S.3}$$

2

with

$$a(\boldsymbol{v}, \tilde{\boldsymbol{v}}) = \int \int 2\mu \left[\mathbf{D_a}(\boldsymbol{v}) : \mathbf{D_a}(\tilde{\boldsymbol{v}}) + \frac{u\tilde{u}}{r^2} \right] r \, \mathrm{d}r \, \mathrm{d}z \qquad \text{(S.4)}$$

$$b(\tilde{\boldsymbol{v}}, p) = \int \int p \left(\nabla_a \cdot \tilde{\boldsymbol{v}} + \frac{\tilde{u}}{r} \right) r \, \mathrm{d}r \, \mathrm{d}z \qquad \text{(S.5)}$$

$$L(\tilde{\boldsymbol{v}}) = \int_\Gamma \tilde{\boldsymbol{v}} \cdot (\boldsymbol{n}_\Gamma \cdot \mathbf{T}) \sqrt{1 + (\partial_r h)^2} \, r \, \mathrm{d}r \,. \qquad \text{(S.6)}$$

While the no-slip boundary condition $\boldsymbol{v} = 0$ at the substrate is strongly imposed, the term L allows to impose Neumann data for the interfacial traction. The Marangoni shear stress in tangential direction can easily be handled in this way, but the normal direction velocity v_n is subject to a Dirichlet boundary condition stemming from the kinematic relation (27). The values for the height evolution $\partial_t h$ and the axial evaporation velocity w_e are taken from the LA simulation. To impose (27) weakly, we employ the method proposed by Nitsche [6] which involves the consideration of additional terms in the bilinear form a and the linear form L. The final weak formulation reads

$$a(\boldsymbol{v}, \tilde{\boldsymbol{v}}) + a'(\boldsymbol{v}, \tilde{\boldsymbol{v}}) - b(\tilde{\boldsymbol{v}}, p) = L'(\tilde{\boldsymbol{v}}) \qquad \text{and} \qquad b(\boldsymbol{v}, \tilde{p}) = 0 \qquad \text{(S.7)}$$

with

$$a'(\boldsymbol{v}, \tilde{\boldsymbol{v}}) = \int_\Gamma \Big[\eta(\boldsymbol{n}_\Gamma \cdot \boldsymbol{v})(\boldsymbol{n}_\Gamma \cdot \tilde{\boldsymbol{v}}) - G(\boldsymbol{v}, p)(\boldsymbol{n}_\Gamma \cdot \tilde{\boldsymbol{v}})$$
$$- \Theta \cdot (\boldsymbol{n}_\Gamma \cdot \boldsymbol{v}) G(\tilde{\boldsymbol{v}}, 0) \Big] \sqrt{1 + (\partial_r h)^2} \, r \, \mathrm{d}r \qquad \text{(S.8)}$$

$$L'(\tilde{\boldsymbol{v}}) = \int_\Gamma \Big[\left(\eta v_n (\boldsymbol{n}_\Gamma \cdot \tilde{\boldsymbol{v}}) - \Theta \cdot v_n G(\tilde{\boldsymbol{v}}, 0) \right) \sqrt{1 + (\partial_r h)^2} - (\partial_r \sigma)(\boldsymbol{t}_\Gamma \cdot \tilde{\boldsymbol{v}}) \Big] r \, \mathrm{d}r \,.$$
$$\text{(S.9)}$$

Here, η is the enforcing constant of the Nitsche method, $\Theta \in \{1, 0, -1\}$ selects its particular implementation [7] and

$$G(\boldsymbol{v}, p) = -p + 2\mu \left(\boldsymbol{n}_\Gamma \cdot \mathbf{D_a}(\boldsymbol{v}) \cdot \boldsymbol{n}_\Gamma \right) \qquad \text{(S.10)}$$

is the normal component of the stress at the interface, i.e. the normal traction. The surface tension gradient $\partial_r \sigma$ stems again from the LA simulation.

The weak form (S.7) was solved on a Taylor-Hood mixed function space using the finite element package FEniCS[1] [8]. The parameter η was set to

---

[1] http://fenicsproject.org

$\eta = \eta_0/r_{\mathrm{tri}}$ where r_{tri} is the circumradius of the element. Due to the choice of $\Theta = -1$, a good convergence is ensured irrespective of the particular value of η_0 [7]. We have validated our FEM implementation by comparing it with the analytical solution for the Stokes flow inside a spherical droplet subject to thermocapillary motion [9].
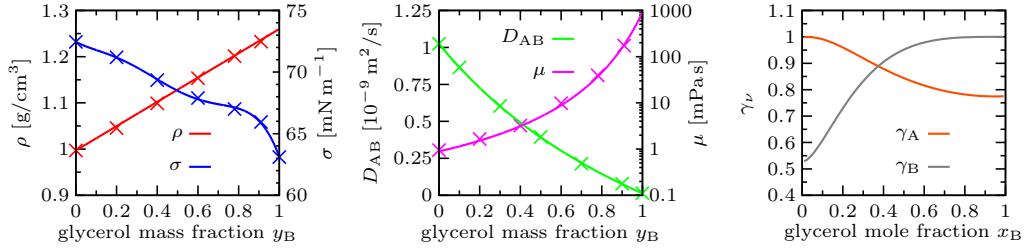
S.3. Composition-dependence of the fluid properties

Figure S.1: Composition-dependence of the physical properties (water-glycerol) at $T = 25\,°C$: According to ref. [10], the mass density ρ can be considered as linear. Their surface tension data was fitted by a fifth order polynomial to model the pronounced slope in the limit of pure glycerol. The variation of the mutual diffusion coefficient D_{AB} [11] and the viscosity μ [10, 12] comprises several orders of magnitude. The activity coefficients γ_ν were determined by *AIOMFAC* [13, 14].
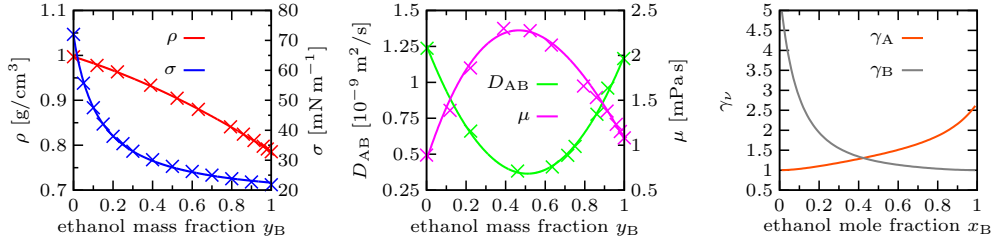

Figure S.2: Composition-dependence of the physical properties (water-ethanol) at $T = 25\,°C$: The experimental data for the mass density ρ of González et al. [15] was fitted by a parabola. Their data for the viscosity μ was fitted by a third order polynomial. The mutual diffusion coefficient D_{AB} was taken from ref. [16] and fitted by a parabola, whereas the surface tension data stems from ref. [17] and was fitted by a shifted reciprocal relation. The activity coefficients γ_ν stem again from *AIOMFAC* calculations.

In order to model the composition-dependence of the mass density ρ, viscosity μ, surface tension σ and diffusivity D_{AB}, experimental data was

4

fitted. The thermodynamic model *AIOMFAC*[2] [13, 14] was used for the determination of the activity coefficients γ_ν. The corresponding data is shown in Figure S.1 and Figure S.2 for water-glycerol and water-ethanol mixtures, respectively.

S.4. Drying with an unpinned contact line

S.4.1. Modeling

The model can easily be generalized to unpinned contact lines. To that end, a precursor film has to be considered to circumvent the so-called Huh-Scriven paradox [18], i.e. the incompatibility of a contact line movement with the imposed no-slip boundary condition $u|_{z=0} = 0$. The precursor film with a thickness of $h^* = h(0,0)/100$ is connected to the droplet profile by adding the disjoining pressure,

$$\Pi = -\frac{\sigma\,\theta_{\mathrm{e}}^2}{2h^*}\frac{(n-1)(m-1)}{(n-m)}\left(\left(\frac{h^*}{h}\right)^n - \left(\frac{h^*}{h}\right)^m\right), \qquad (S.11)$$

with $n = 3$ and $m = 2$, to the pressure, i.e $p = p_{\mathrm{L}} + \Pi$ [19]. The equilibrium contact angle θ_{e} depends on the composition at the contact line. Here, we use the model proposed by Kwok & Neumann [20] which has been derived from a combination of the Young equation, fitting of experimental data and a modified version of the combining rule of Berthelot for the interaction energy [21]. Assuming that there is no preferential adsorption of one liquid component at the substrate, this model can be applied to mixtures. The contact angle θ_{e} is accordingly given by

$$\cos\theta_{\mathrm{e}} = -1 + 2\sqrt{\frac{\sigma_{\mathrm{sg}}}{\sigma_{\mathrm{lg}}}}\exp\left(-\beta\left(\sigma_{\mathrm{sg}} - \sigma_{\mathrm{lg}}\right)^2\right). \qquad (S.12)$$

Here, $\beta = 124.7\,\mathrm{m^4/J^2}$ was used, $\sigma_{\mathrm{lg}}(r,t) = \sigma(r,t)$ is the surface tension between liquid and vapor phase at the contact line and σ_{sg} is the surface tension between gas phase and substrate. The latter is a constant that does not depend on the liquid composition and can be estimated by solving (S.12) for σ_{sg} with an initially prescribed contact angle θ_{e}.

S.4.2. Water-glycerol droplets

Eq. (S.12) has no real solution for θ_{e} in the limit of pure glycerol, if the flat water-glycerol droplets of section 3 with $\theta_{\mathrm{e}}(t{=}0) = 25°$ and an unpinned

---
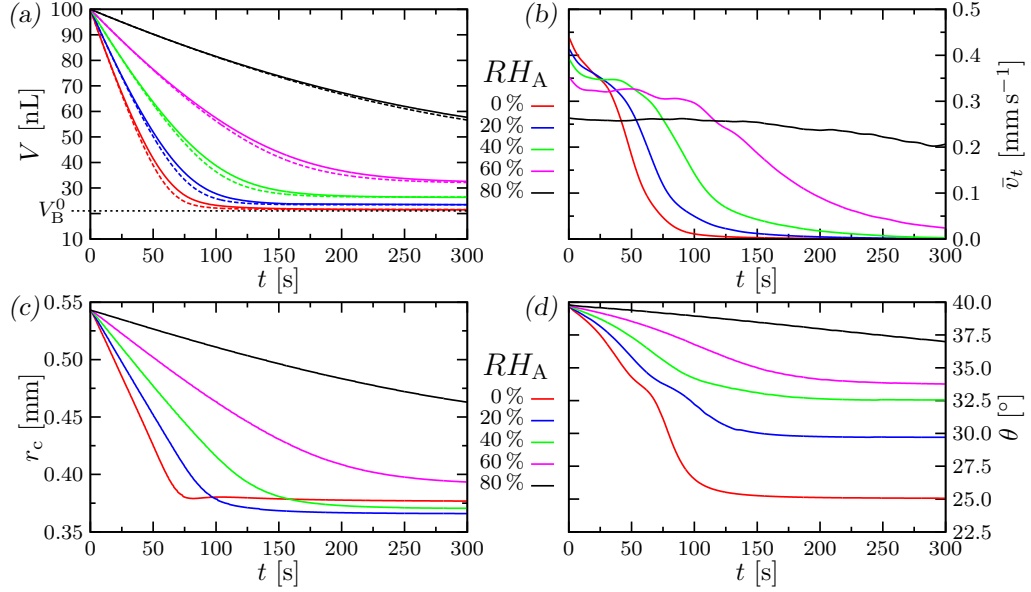
[2]http://www.aiomfac.caltech.edu

Figure S.3: Evolution of $100\,\mathrm{nL}$ droplets ($75\,\%$ water $+$ $25\,\%$ glycerol in terms of mass fractions) with an unpinned contact line and $\theta(t{=}0) = 40°$ at different relative humidities (solid lines). (a) volume evolution, where the dashed lines indicate the corresponding data with a pinned contact line of Figure 3. (b) averaged tangential interface velocity $\bar{v}_t$. (c) base radius r_c. (d) contact angle θ.

contact line are considered. The fact that no real solution exists for high glycerol mass fractions means that complete wetting occurs at later times. In order to have a well defined contact line during the entire simulation, a higher initial contact angle of $\theta_\mathrm{e}(t{=}0) = 40°$ is used in the following. Due to the high contact angle, the generalized lubrication approximation (cf. section 4.2.2) was used.

In Figure S.3, the corresponding results are depicted. At a given volume V, the area of the liquid-air interface of a droplet with an unpinned contact line (solid lines) is smaller than of the corresponding droplet with a pinned contact line (dashed lines). As a consequence, the total evaporation rate is reduced for the unpinned contact line, which is also apparent from Figure S.3(a).

In contrast to the droplets with an initial contact angle of $\theta_\mathrm{e}(t{=}0) = 25°$ (cf. section 3), the deviation from the spherical cap shape is less pronounced for $\theta_\mathrm{e}(t{=}0) = 40°$. This can also be inferred from Figure S.3(c) and Figure S.3(d), which show a monotonic decrease of the contact line radius $r_\mathrm{c}(t)$

and the contact angle $\theta(t)$, respectively. Only for dry air ($RH_A = 0$), a slight minimum can be seen in the graph of $r_c(t)$, which is the result of an insignificant deformation. For flatter droplets with lower initial contact angles, the deformation from a spherical cap is far more pronounced, which leads to highly non-monotonic evolutions of $r_c(t)$ and $\theta(t)$.

Due to the different final compositions of the droplets at different humidities, the remaining droplet will be flatter for lower humidities (cf. Figure S.3(d)). Since the base radius r_c depends on the volume V and the contact angle θ, the final value of r_c does not show a strict monotonic behavior as a function of the humidity RH_A (cf. Figure S.3(c)).

S.4.3. Water-ethanol droplets

The evolution of a $100\,\mathrm{nL}$ droplet initially consisting of $80\,\%$ water $+ 20\,\%$ ethanol in terms of mass fractions with an initial equilibrium contact angle $\theta_e = 20°$ and an unpinned contact line is depicted in Figure S.4. While the ethanol content evaporates, the unpinned contact line recedes quickly due to the increasing equilibrium contact angle θ_e according to (S.12). When the ethanol has almost entirely evaporated, the Marangoni flow ceases and the remaining water droplet evaporates with a high contact angle $\theta_e \approx 78°$. Although the flow velocity will be rather inaccurate in this regime due to the lubrication approximation (cf. section 5.1), the evaporation rate and thereby the volume evolution are still exact. Since the generalized lubrication approximation was used here (cf. section 4.2.2), the droplet is in a spherical cap shape.

While the compositional receding in the early stages is faster than the theoretically derived relation $r_c \propto \sqrt{t_{\mathrm{dry}} - t}$ for pure fluids [22], the evaporative receding of the remaining water droplet at later times coincides with the theoretical prediction (cf. Figure S.4(f)).

A receding contact line with a drastically increasing contact angle was also observed in experiments [23–25]. However, an initial decrease of the contact angle was also noticed in these experiments, whereas our model does not exhibit this behavior. Since the initial contact angle decrease is attributed to the volume loss at an initially pinned contact line, this effect could be incorporated into our model by considering contact angle hysteresis, i.e. an initially pinned contact line until the actual contact angle falls below a specific composition-dependent receding contact angle.
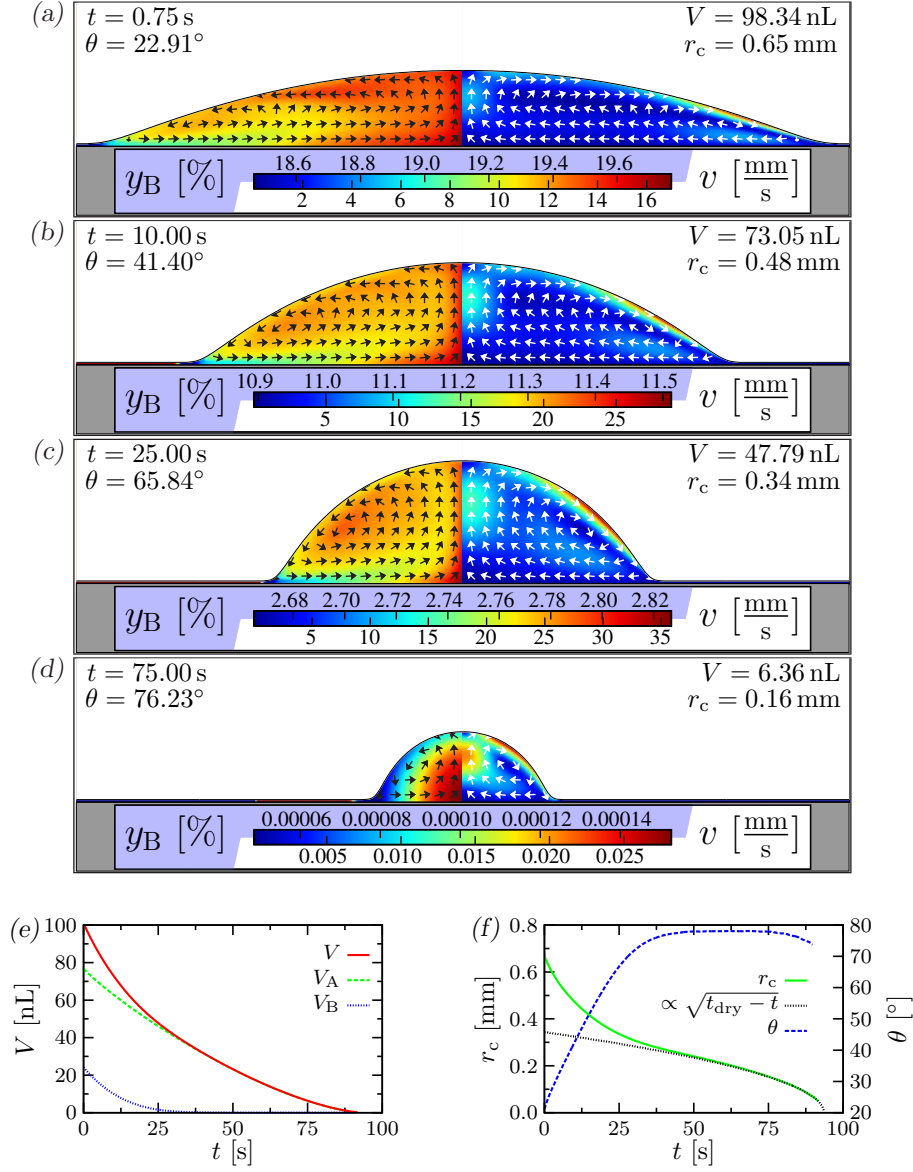
Figure S.4: Evaporation of a 100 nL droplet (initially 80 % water + 20 % ethanol in terms of mass fractions) in dry ambient air with an unpinned contact line at different times. (a-d) the ethanol mass fraction y_B (left side) and the velocity (right side) are shown. The flow direction is indicated by the arrows. (e) shows the total volume (solid lines) and partial (dashed/dotted lines) volumes. (f) The receding contact line radius $r_c(t)$ initially differs from the relation $\propto \sqrt{t_{dry} - t}$. Furthermore, the steep increase of the contact angle is shown.

S.5. Evaporation rate

In the following, additional information regarding the evaporation rate of mixture droplets are discussed. To keep it most general and valid for arbitrary contact angles, this is done without taking the lubrication theory limit $h \to 0$. In Figure S.5, the impact of the liquid composition on the evaporation rate is depicted. For an inhomogeneous composition along the liquid-air interface, the evaporation rate of one species ν can be strongly enhanced at positions with locally elevated mole fractions x_ν in the liquid. On the contrary, condensation may happen even for dry air at positions with locally lower liquid mole fraction.
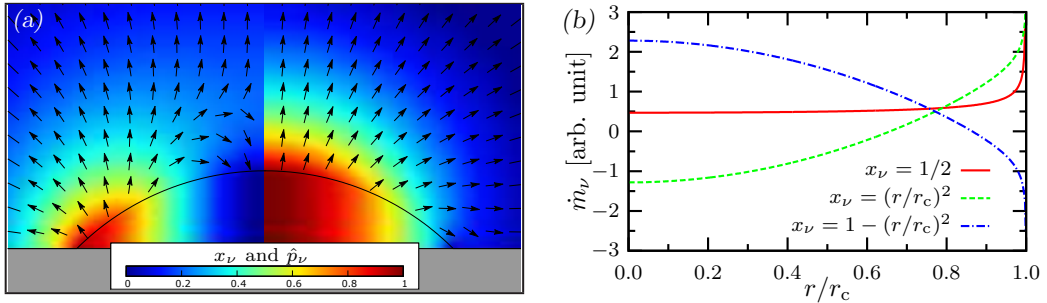

Figure S.5: (a) Droplet with an artificial liquid composition $x_\nu = (r/r_c)^2$ (left) and $x_\nu = 1 - (r/r_c)^2$ (right) and the corresponding reduced vapor pressure $\hat{p}_\nu$ in the air according to Eqs. (12) and (13) with $RH_\nu = 0$. The activity coefficients γ_ν were set to unity and the arrows indicate the vapor diffusion direction. (b) Comparison of the resulting reduced mass transfer rates $\dot{m}_\nu$ for both non-uniform compositions of (a) (dashed lines) and a homogeneous interface $x_\nu = 1/2$ (solid line).

S.5.1. Analytical solution for the evaporation rate of a sessile mixture droplet

Here, an analytical solution for the evaporation rate of binary mixture droplets is presented. For simplicity, the component index ν is dropped in the following. According to (12), one has to solve $\nabla^2 \hat{p} = 0$ subject to the boundary conditions (15), (16) and (17). The droplet surface $h(r,t)$ is assumed to have a spherical cap shape.

The solution of the Laplace equation $\nabla^2 \hat{\rho} = 0$ with a Dirichlet boundary along a spherical cap can be solved in toroidal coordinates (α, β) [26–29]:

$$r = r_c \frac{\sinh \alpha}{\cosh \alpha - \cos \beta}, \qquad z = r_c \frac{\sin \beta}{\cosh \alpha - \cos \beta}. \tag{S.13}$$

9

The liquid-air interface is now given by $\beta = \beta_0 = \pi - \theta$ and $\alpha \in [0, \infty)$, where $\alpha = 0$ holds at the apex $(r = 0)$ and the contact line $(r = r_c)$ is reached in the limit $\alpha \to \infty$. Following the derivation of Lebedev [26], the boundary condition at the liquid-air interface is decomposed into the value $b_c = (\gamma x)|_{\alpha \to \infty, \beta = \beta_0}$ at the contact line and the deviation from it, $b_\Delta(\alpha) = \gamma(\alpha)x(\alpha) - b_c$. The solution of $\nabla^2 \hat{p} = 0$ subject to the afore-mentioned boundary conditions is separated in the same manner:

$$\hat{p}(\alpha, \beta) = RH + (b_c - RH)\, \hat{p}_c(\alpha, \beta) + \hat{p}_\Delta(\alpha, \beta) \tag{S.14}$$

with

$$\hat{p}_c(\alpha, \beta) = N(\alpha, \beta) \int_0^\infty \mathrm{d}\tau\, K(\tau, \beta) C_\tau(\alpha) \frac{\cosh(\theta\tau)}{\cosh(\pi\tau)} \tag{S.15}$$

$$\hat{p}_\Delta(\alpha, \beta) = N(\alpha, \beta) \int_0^\infty \mathrm{d}\tau\, K(\tau, \beta) C_\tau(\alpha) \mathcal{M}(\tau) \tag{S.16}$$

$$N(\alpha, \beta) = \sqrt{2 \cosh\alpha - 2\cos\beta} \tag{S.17}$$

$$K(\tau, \beta) = \frac{\cosh((2\pi - \beta)\tau)}{\cosh((\pi - \theta)\tau)} \tag{S.18}$$

$$C_\tau(\alpha) = P_{-1/2+i\tau}(\cosh\alpha) \tag{S.19}$$

$$\mathcal{M}(\tau) = \tau \tanh(\pi\tau) \int_0^\infty \mathrm{d}\alpha' \frac{b_\Delta(\alpha') C_\tau(\alpha') \sinh\alpha'}{\sqrt{2\cosh\alpha' + 2\cos\theta}} \tag{S.20}$$

Here, $P_{-1/2+i\tau}$ are the conical functions, i.e. Legendre functions of the first kind with a fractional complex index, and $\mathcal{M}$ is the so-called Mehler-Fock transformation of b_Δ [30].

The part $\hat{p}_c$ actually solves $\nabla^2 \hat{p}_c = 0$ with the constant boundary condition $\hat{p}_c = 1$ at Γ and $\hat{p}_c = 0$ far away from the droplet, i.e. it resembles the vapor distribution around a pure liquid droplet with $RH = 0$ (see refs. [27, 28]), whereas the contribution $\hat{p}_\Delta$ arises from a non-uniform interface concentration. For the evaporation rate (12), the normal derivative of $\hat{p}$ at the interface has to be evaluated, which reads [28]

$$-\nabla\hat{p} \cdot \boldsymbol{n}_\Gamma = \frac{\cosh\alpha - \cos\beta}{r_c} \, \partial_\beta \hat{p}|_{\beta = 3\pi - \theta} \,. \tag{S.21}$$

The mass loss $\dot{m}$ can finally be expressed by

$$\dot{m}(\alpha) = \frac{D^g M p_{\mathrm{sat}}}{r_c R_u T} \left[(b_c - RH)\, \hat{J}_c(\alpha) + \hat{J}_\Delta(\alpha) \right] \tag{S.22}$$

10

with

$$\hat{J}_c(\alpha) = \frac{\sin\theta}{2} + N'(\alpha)\int_0^\infty \mathrm{d}\tau K'(\tau)C_\tau(\alpha)\frac{\cosh(\theta\tau)}{\cosh(\pi\tau)} \tag{S.23}$$

$$\hat{J}_\Delta(\alpha) = \frac{\sin\theta}{2}b_\Delta(\alpha) + N'(\alpha)\int_0^\infty \mathrm{d}\tau K'(\tau)C_\tau(\alpha)\mathcal{M}(\tau) \tag{S.24}$$

$$N'(\alpha) = \sqrt{2}\left(\cosh\alpha + \cos\theta\right)^{3/2} \tag{S.25}$$

$$K'(\tau) = \tau\tanh((\pi-\theta)\tau) \tag{S.26}$$

The portion proportional to $\hat{J}_c$ is the evaporation rate of a droplet with a constant interface composition $b = b_c$, whereas $\hat{J}_\Delta$ stems from non-uniformities of the concentration. The portion $\hat{J}_c$ can be written in terms of conventional functions only [29]:

$$\hat{J}_c(\alpha) = \frac{\pi N'(\alpha)}{2\sqrt{2}(\pi-\theta)^2}\int_\alpha^\infty \mathrm{d}x \frac{\tanh\left(\frac{\pi x}{2(\pi-\theta)}\right)}{\cosh\left(\frac{\pi x}{2(\pi-\theta)}\right)\sqrt{\cosh x - \cosh\alpha}} . \tag{S.27}$$

S.5.2. Boundary element method

From a numerical point of view, the forward and backward Mehler-Fock transformations (S.20) and (S.24), respectively, show rather poor convergence and require a very fine integral discretization. This disadvantage can be overcome by invoking a more suitable boundary element method. Geometric singularities are problematic in the latter, but the contact line singularity is already resolved in $\hat{J}_c$, which can be evaluated numerically according to (S.27) by the substitution $x = 2\operatorname{arcosh}(\cosh(\alpha/2)\cosh y)$ [29]. $\hat{J}_\Delta$ is solved by considering a single layer potential representation of $\hat{p}_\Delta$, which reads in Cartesian coordinates

$$\hat{p}_\Delta(\boldsymbol{r}_0) = \frac{1}{r_c}\int_{\Gamma\cup\Gamma^-} G(\boldsymbol{r}_0,\boldsymbol{r})s(\boldsymbol{r})\mathrm{d}A(\boldsymbol{r}) \tag{S.28}$$

Here, $G(\boldsymbol{r}_0,\boldsymbol{r}) = (4\pi\|\boldsymbol{r}_0 - \boldsymbol{r}\|)^{-1}$ is the Green's function and $s(\boldsymbol{r})$ is a yet unknown surface density on the spherical cap Γ and its corresponding counterpart Γ^- mirrored at the plane $z = 0$. The latter is introduced to fulfil the no-penetration boundary condition $\partial_z\hat{p}_\Delta|_{z=0} = 0$ by the method of images. Imposing $\hat{p}_\Delta(\boldsymbol{r}_0) = b_\Delta(\boldsymbol{r}_0)$ as principal value directly on the surface

11

$\Gamma \cup \Gamma^-$ and switching to axisymmetric cylindrical coordinates, one obtains a Fredholm integral equation of the first kind for $s(r)$ [31]:

$$b_\Delta(r_0) = \frac{2}{\pi r_c} \int_0^{r_c} dr \, r \sqrt{1 + (\partial_r h)^2} \, [F(h_0 - h, r, r_0) + F(h_0 + h, r, r_0)] \, s(r)$$

(S.29)

$$\text{with} \quad F(h \pm h_0, r, r_0) = \frac{K\left(\frac{4rr_0}{(h \pm h_0)^2 + (r + r_0)^2}\right)}{\sqrt{(h \pm h_0)^2 + (r + r_0)^2}}.$$

(S.30)

Here, K is the complete elliptic integral of the first kind and the abbreviations $h = h(r, t)$ and $h_0 = h(r_0, t)$ were used. The surface density $s(r)$ is discretized and (S.29) is integrated piecewise by a high order Gauss-Legendre quadrature on the interpolated droplet shape $h(r, t)$. The inversion of the corresponding matrix yields the surface density $s(r)$ and, finally, with the discontinuity

$$\hat{J}_\Delta(r) = s(r) + \frac{1}{2} b_\Delta(r),$$

(S.31)

the term $\hat{J}_\Delta(r)$ is obtained.

It is straightforward to determine the corresponding expressions for the lubrication approximation by considering the limit $h \to 0$.

S.5.3. Validity of the quasi-steady vapor diffusion assumption

For the evaporation rate $\dot{m}_\nu$ in (12), it was assumed that the vapor diffusion can be treated in its quasi-steady limit, i.e. by the Laplace equation $\nabla^2 \hat{p}_\nu = 0$. For a pure fluid, this was already validated by Deegan et al. [27] and Hu & Larson [32]. The drying time τ_{dry} of the droplet, i.e. the characteristic time for a geometric change of the gas domain, is about 10^5 times larger than the vapor diffusion timescale $\tau_{\text{vapor}} = r_c^2 / D_{\nu C}^g$. For pure water, this evaporation model has successfully been used to reproduce the experimental data for evaporating water droplets over a wide range of contact angles [33].

In the case of mixtures, however, not only the geometric domain for $\nabla^2 \hat{p}_\nu = 0$ changes over time, but also the imposed boundary condition (17), i.e. the vapor-liquid equilibrium at the droplet surface. Since the mutual diffusion coefficient in the liquid mixture is about four to five orders of magnitude smaller than the vapor diffusivity, a comparably fast liquid diffusion can be ruled out. Due to the strong coupling of evaporation and the driven Marangoni flow, however, an a priori estimation of the convective time scale
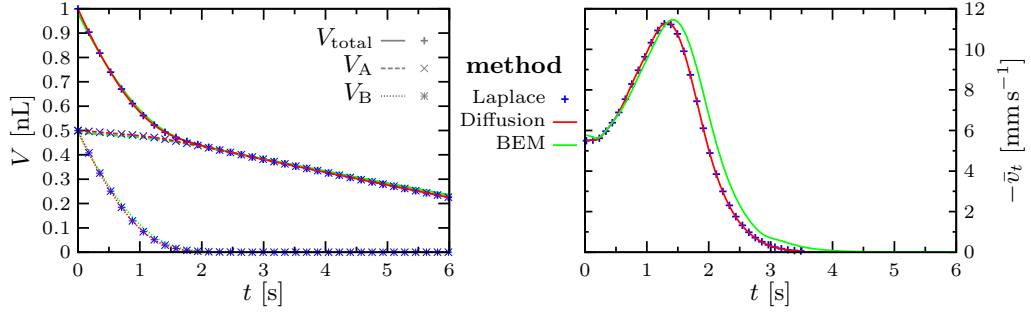
12

Figure S.6: Validation of the quasi-steady evaporation model on the basis of a $100\,\mathrm{nL}$ water-ethanol droplet ($50\,\%$ water $+$ $50\,\%$ ethanol in terms of mass fractions) with a pinned contact line, $RH_\mathrm{A} = 80\,\%$, $RH_\mathrm{B} = 0\,\%$ and $\theta(t{=}0) = 25°$: The full vapor diffusion model (blue symbols) is perfectly approximated by the quasi-steady Laplace equation (red lines). Deviations from the boundary element method (green lines) are due to the restriction to finite domain sizes of the former two.

τ_conv is not feasible. Therefore, the convective time scale was evaluated based on our numerical results by $\tau_\mathrm{conv} = r_\mathrm{c}/|\bar{v}_t|$.

For the investigated water-glycerol droplets of section 3, the characteristic time of convection τ_conv is about two orders of magnitude larger than τ_vapor, but for the presented water-ethanol droplets, the maximum determined ratio reads $\tau_\mathrm{vapor}/\tau_\mathrm{conv} \approx 0.66$ (evolution with $RH_\mathrm{A} = 80\,\%$ of Figure 5). Hence, the accuracy of the generalized quasi-steady evaporation model is questionable in this case.

In order to validate the quasi-steady model for the representative binary mixture droplets in this article, the droplet evolution based on the instantaneous Laplace equation $\nabla^2 \hat{p}_\nu = 0$ was compared with the corresponding one with a spatio-temporal vapor diffusion equation $\partial_t \hat{p}_\nu = D_{\nu\mathrm{C}}^\mathrm{g} \nabla^2 \hat{p}_\nu$. For the latter case, the stationary solution was used as initial condition at $t = 0$. In Figure S.6 the resulting volume evolutions and the averaged tangential interface velocity $\bar{v}_t$ for the spatio-temporal model (red lines) and the approximated quasi-steady model (blue symbols) are depicted. It is apparent that the data collapses perfectly. Thus, the quasi-steady evaporation model is conclusively substantiated for the presented droplet evolutions. Furthermore, the corresponding result of the boundary element method of appendix S.5.2, which was used throughout this article, is depicted with almost perfect agreement in Figure S.6 (green lines).

[1] A. Gil, J. Segura, N. M. Temme, An improved algorithm and a Fortran

90 module for computing the conical function, Comput. Phys. Commun. 183 (3) (2012) 794–799. doi:10.1016/j.cpc.2011.11.025.

[2] Y. Shapira, Matrix-based multigrid theory and applications, Springer, New York, NY, 2008.

[3] R. Alexander, Diagonally implicit Runge–Kutta methods for stiff O.D.E.'s, SIAM J. Numer. Anal. 14 (6) (1977) 1006–1021. doi:10.1137/0714068.

[4] L. M. Skvortsov, Diagonally implicit Runge-Kutta methods for stiff problems, Comput. Math. and Math. Phys. 46 (12) (2006) 2110–2123. doi:10.1134/s0965542506120098.

[5] Z. Belhachmi, C. Bernardi, S. Deparis, Weighted Clément operator and application to the finite element discretization of the axisymmetric Stokes problem, Numerische Mathematik 105 (2) (2006) 217–247. doi:10.1007/s00211-006-0039-9.

[6] J. Nitsche, Über ein Variationsprinzip zur Lösung von Dirichlet-Problemen bei Verwendung von Teilräumen, die keinen Randbedingungen unterworfen sind, Abh. Math. Semin. Univ. Hambg. 36 (1) (1971) 9–15. doi:10.1007/bf02995904.

[7] F. Chouly, P. Hild, Y. Renard, Symmetric and non-symmetric variants of nitsche's method for contact problems in elasticity: theory and numerical experiments, Math. Comp. 84 (293) (2014) 1089–1112. doi:10.1090/s0025-5718-2014-02913-x.

[8] A. Logg, Automated solution of differential equations by the finite element method the FEniCS book, Springer, Berlin New York, 2012.

[9] N. O. Young, J. S. Goldstein, M. J. Block, The motion of bubbles in a vertical temperature gradient, J. Fluid Mech. 6 (03) (1959) 350. doi:10.1017/s0022112059000684.

[10] K. Takamura, H. Fischer, N. R. Morrow, Physical properties of aqueous glycerol solutions, J. Petrol. Sci. Eng. 98-99 (2012) 50–60. doi:10.1016/j.petrol.2012.09.003.

[11] G. D'Errico, O. Ortona, F. Capuano, V. Vitagliano, Diffusion coefficients for the binary system glycerol + water at 25 °C. A velocity correlation study, J. Chem. Eng. Data 49 (6) (2004) 1665–1670. doi:10.1021/je049917u.

[12] N.-S. Cheng, Formula for the viscosity of a glycerol–water mixture, Ind. Eng. Chem. Res. 47 (9) (2008) 3285–3288. doi:10.1021/ie071349z.

[13] A. Zuend, C. Marcolli, B. P. Luo, T. Peter, A thermodynamic model of mixed organic-inorganic aerosols to predict activity coefficients, Atmos. Chem. Phys. 8 (16) (2008) 4559–4593. doi:10.5194/acp-8-4559-2008.

[14] A. Zuend, C. Marcolli, A. M. Booth, D. M. Lienhard, V. Soonsin, U. K. Krieger, D. O. Topping, G. McFiggans, T. Peter, J. H. Seinfeld, New and extended parameterization of the thermodynamic model AIOM-FAC: calculation of activity coefficients for organic-inorganic mixtures containing carboxyl, hydroxyl, carbonyl, ether, ester, alkenyl, alkyl, and aromatic functional groups, Atmos. Chem. Phys. 11 (17) (2011) 9155–9206. doi:10.5194/acp-11-9155-2011.

[15] B. González, N. Calvar, E. Gómez, A. Domínguez, Density, dynamic viscosity, and derived properties of binary mixtures of methanol or ethanol with water, ethyl acetate, and methyl acetate at T=(293.15, 298.15, and 303.15)K, J. Chem. Thermodyn. 39 (12) (2007) 1578–1588. doi:10.1016/j.jct.2007.05.004.

[16] S. Pařez, G. Guevara-Carrion, H. Hasse, J. Vrabec, Mutual diffusion in the ternary mixture of water + methanol + ethanol and its binary subsystems, Phys. Chem. Chem. Phys. 15 (11) (2013) 3985. doi:10.1039/c3cp43785j.

[17] G. Vazquez, E. Alvarez, J. M. Navaza, Surface tension of alcohol water + water from 20 to 50 °C, J. Chem. Eng. Data 40 (3) (1995) 611–614. doi:10.1021/je00019a016.

[18] C. Huh, L. E. Scriven, Hydrodynamic model of steady movement of a solid/liquid/fluid contact line, J. Colloid Interf. Sci. 35 (1) (1971) 85–101. doi:10.1016/0021-9797(71)90188-3.

[19] L. W. Schwartz, R. R. Eley, Simulation of droplet motion on low-energy and heterogeneous surfaces, J. Colloid Interf. Sci. 202 (1) (1998) 173–188. doi:10.1006/jcis.1998.5448.

[20] D. Y. Kwok, A. W. Neumann, Contact angle interpretation in terms of solid surface tension, Colloid. Surface. A 161 (1) (2000) 31–48. doi:10.1016/s0927-7757(99)00323-4.

[21] D. Berthelot, Sur le mélange des gaz, Compt. Rendus 126 (1898) 1703–1706.

[22] N. Shahidzadeh-Bonn, S. Rafaï, A. Azouni, D. Bonn, Evaporating droplets, J. Fluid Mech. 549 (-1) (2006) 307. doi:10.1017/s0022112005008190.

[23] K. Sefiane, L. Tadrist, M. Douglas, Experimental study of evaporating water-ethanol mixture sessile drop: influence of concentration, Int. J. Heat Mass Trans. 46 (23) (2003) 4527–4534. doi:10.1016/s0017-9310(03)00267-9.

[24] A. K. H. Cheng, D. M. Soolaman, H.-Z. Yu, Evaporation of microdroplets of ethanol–water mixtures on gold surfaces modified with self-assembled monolayers, J. Phys. Chem. B 110 (23) (2006) 11267–11271. doi:10.1021/jp0572885.

[25] L. Shi, P. Shen, D. Zhang, Q. Lin, Q. Jiang, Wetting and evaporation behaviors of water–ethanol sessile drops on PTFE surfaces, Surf. Interface Anal. 41 (12-13) (2009) 951–955. doi:10.1002/sia.3123.

[26] N. N. Lebedev, Special functions and their applications, Dover Publications, New York, 1972.

[27] R. Deegan, O. Bakajin, T. Dupont, G. Huber, S. Nagel, T. Witten, Contact line deposits in an evaporating drop, Phys. Rev. E 62 (1) (2000) 756–765. doi:10.1103/physreve.62.756.

[28] Y. Popov, Evaporative deposition patterns: Spatial dimensions of the deposit, Phys. Rev. E 71 (3). doi:10.1103/physreve.71.036313.

[29] A. Liemert, Explicit solution for the electrostatic potential of the conducting double sphere, J. Appl. Phys. 115 (16) (2014) 164907. doi:10.1063/1.4873296.

[30] F. G. Mehler, Ueber eine mit den Kugel- und Cylinderfunc-tionen verwandte Function und ihre Anwendung in der Theorie der Elektricitätsvertheilung, Math. Ann. 18 (2) (1881) 161–194. doi:10.1007/bf01445847.

[31] C. Pozrikidis, Introduction to theoretical and computational fluid dynamics, Oxford University Press, New York, 1979.

[32] H. Hu, R. G. Larson, Evaporation of a sessile droplet on a substrate, J. Phys. Chem. B 106 (6) (2002) 1334–1344. doi:10.1021/jp0118322.

[33] H. Gelderblom, A. G. Marín, H. Nair, A. van Houselt, L. Lefferts, J. H. Snoeijer, D. Lohse, How water droplets evaporate on a superhydrophobic substrate, Phys. Rev. E 83 (2). doi:10.1103/physreve.83.026306.